Experimental and numerical investigation of ballistic performance of Kevlar-29 / Ceramic (SiC) armor system

Experimental and numerical investigation of ballistic performance of Kevlar-29 / Ceramic (SiC) armor system

M M Semman[1], N A Azab[1], Mostafa Shazly[2], Mohamed Hazem Abdel Latif [1] and A Fayed [3]

[1] Design and Production Engineering Department, Faculty of Engineering, Ain Shams University, Cairo, Egypt
[2] Mechanical Engineering Department, Faculty of Engineering, The British University in Egypt, Al-Shorouk City, Cairo, Egypt
[3] Material Science and Technology department, Military Technical College, Cairo, Egypt

Mustafa.Semman@gmail.com

Abstract. The requirement to protect the personnel against 7.62 x 54 mm API ammunition and facilitate the user's ability to move made it necessary to improve the lightweight armors. One of the primary modifications made for these armors is the use of ceramics with high hardness and low weight. The ballistic performance is improved by using these ceramics as the front layer of the armor. The current study looks into how employing Silicon Carbide tiles can improve an ARMOX 500T armor's ballistic performance against 7.62 x 54 mm API ammunition and reduce its aerial density by about 70%. In order to reduce the required number of laboratory experiments, FEA models have been built, and results have been verified through comparisons with laboratory experiments.

Keywords. ARMOX 500T, Kevlar, Silicon Carbide, FEA, Johnson-Cook model, Hashin damage, Johnson-Holmquist (JH2) model, 7.62 x 54 mm API, Ballistic performance.

1. Introduction

Composite bilayer armor structures, which consist of a front brittle layer and a tough back plate, are broadly used in today's lightweight armors [1], to withstand different threats of ammunition. The front layer, which is usually a ceramic layer (Alumina, Boron Carbide, etc.) with low density, high compressive strength and hardness, has a preeminent role in distorting the projectile's tip. On the other hand, the backing plate (Steel, Kevlar-29 ….etc.) aims to dissipate the remaining projectile's kinetic energy. When the projectile's tip is eroded by a front hard and brittle ceramic layer, the hard steel core is broken and its cross-sectional area is increased, so, it becomes easier to be stopped by the backing plate. Also, the backing plate in conjunction with the adhesive material aims to constrain the ceramic fragments after impact which prolongs the lifetime of the armor.

In order to investigate the deformation and failure mechanisms of fiber-reinforced composites in layered composite armor against Armor-Piercing ammunition, several experimental and numerical analyses are conducted. For example, Shah Alam et al. [1] used 7.62 mm APM2 ammunition at different velocities to study the ballistic performance of layered composite armors.

Shaker et al. [2] reported using a layer of ceramic to the existing design to enhance the ballistic performance of the bare steel armor in the Kevlar-29 / epoxy composite target.

The developments in finite element analysis and commercial software packages assisted in the advancement in the design and manufacturing of composite armors. These advancements are associated with the development of complex materials models to describe the behavior of different constituents of the armor. In particular, the numerical simulation of brittle material's behavior during bullet penetration necessitates the determination of several material parameters. In addition, a failure criterion for each material within the armor system should be identified to investigate the impact of process-related fracture behavior. In that direction, Senthil1 et al. [3] conducted FEA simulations of AP projectiles against mild steel armor. Similarly, Abou-Elela et al. [4] described the penetration of a high-speed projectile into a metallic bi-element target, consisting of a finite thickness metallic layer facing a semi-infinite RHA armor. On the other hand, Fayed et al. [5] investigated the performance of four different textile materials used as an outer shell of the Silicon Carbide vest to achieve the desired degree of protection against 7.62 x 54 mm caliber.

Since calibers 7.62 x 54 mm are one of the most common calibers, Fayed [8] studied their penetration ability against modern lightweight armor.

In these FEA simulations of the armor penetration process, two primary numerical methodologies have been utilized to simulate the penetration and erosion behavior of high-velocity projectiles fired on ballistic armor. The first is the Lagrangian FE approach, which is the most popular method, where the material's fracture is modeled by a specified fracture criterion and elements deletion technique to eliminate failed and highly distorted elements. However, Gregori et al. [6] compared the results obtained from two different procedures, first is the interaction simulation between armor and 7.62 mm Ball projectile by the implementation of the modified Bernoulli equation and estimation of the absorbed energy in the backing plate by the implementation of an energy formulation based on the wave propagation theory. The second is a full-Lagrangian FEA using LS-DYNA software. Both models had good agreement with the laboratory tests.

The other technique is the smoothed particle hydrodynamics (SPH) method, which does not require element erosion criterion nor does distortion control as compared to the former method, but it suffers from particle inconsistency, tensile instability problem, and its high computational cost as compared to the first technique. Meng et al. [7] applied the SPH approach to study the High-Velocity Impact (HVI) mechanism in order to enhance the ballistic performance of the lightweight armors subjected to HVI. In general, these simulations provide the possibility of conducting a large number of FEA experiments and obtaining results that resemble those obtained from experimental work, thus cutting the time and cost of developing an optimum design for the final product. In the present work, a comparison between a bare ARMOX 500T armors with 16 mm thicknesses and a composite bilayer Kevlar/Silicon Carbide armor structure is conducted experimentally and modeled by Lagrangian FE approach to investigate the enhancement of the ballistic performance and the reduction in aerial density against 7.62 x 54 mm API projectiles.

2. Methodology

2.1. Experimental Work

2.1.1. Materials. The current study is conducted to compare the ballistic performance of two different Armors against 7.62 x 54 mm API ammunition. The first is a bare steel armor while the second is a composite bilayer Armor structure consisting of Kevlar-29 and Silicon Carbide layers. Standard 7.62 x 54 mm API projectile used in the present work is shown in Figure 1. The projectile's length is 33.4 mm and weighs 9.6 g, of which 5.67 g is a hard steel core. This core material has an initial yield strength of 1.2 GPa [8], and a fracture strength of 2.3 GPa at the strain of 2–3% according to Chocron et al. [9]. The constitutive models of the projectile's materials were obtained from the study of Anderson et al. [10].

In the bilayer structure, Kevlar-29 is chosen as the backing plate based on its excellent mechanical properties specifically, good thermal and chemical resistance, high moisture resistance, and high strength-to-weight ratio.

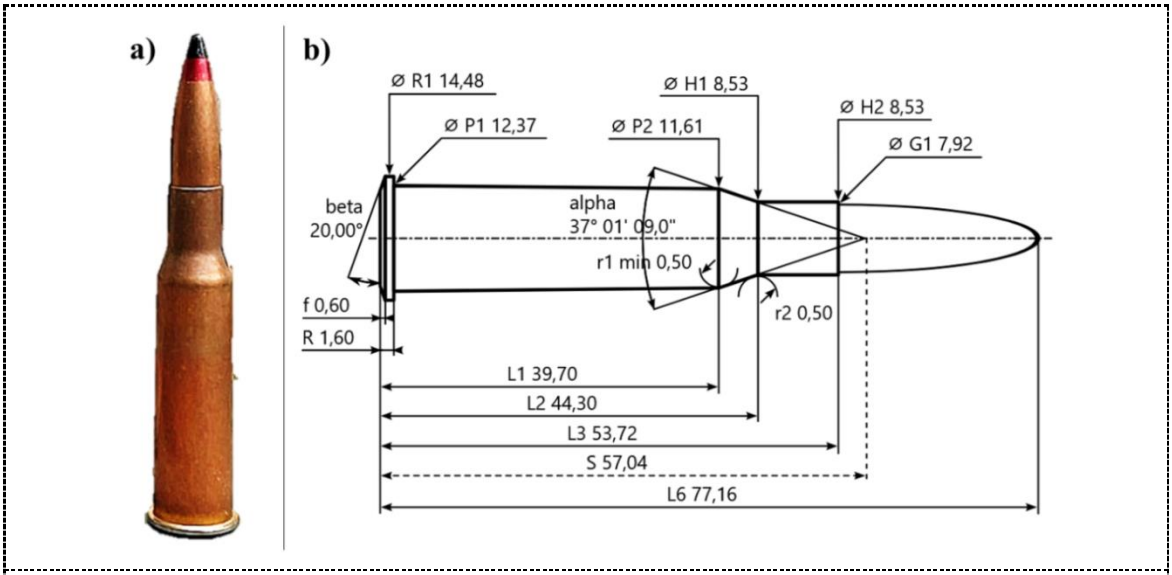

Figure 1. (a) 7.62 x 54 mm API ammunition used in the present work, (b) detail drawing of 7.62 x 54 mm API projectile (all dimensions in mm)

The Silicon Carbide tile was selected as the front layer because of its excellent properties including high thermal conductivity, high strength and hardness, and high resistance to wear and oxidation. The following are the mechanical properties of the used tiles: density equals 3215 Kg/m^3, tensile strength equals 0.37 GPa, Young's modulus equals 449 GPa and Poisson's ratio equals 0.16 [16]. The Silicon Carbide is attached to the Kevlar-29 plate using Polyurethane as an adhesive layer. The nature of polyurethanes allows them to be molded into unusual shapes, and to be used in coatings, adhesives, sealants, and elastomers (CASE) applications. Specifically, Polyurethane adhesives can provide strong bonding advantages.

2.1.2. Preparation of the specimens. In the present work, the first specimen is a bare ARMOX 500T plate having dimensions of 200 × 200 mm and a thickness of 16 mm. Therefore, its areal density equals 126 kg/m^2 as shown in Figure 2a. The second armor is a composite bilayer armor structure consisting of Kevlar-29 / epoxy as a backing plate and Silicon Carbide tiles as a front layer, both layers are joined together with a polyurethane layer. The front layer has a 9 mm thickness Silicon Carbide tile within an area of 180 × 180 mm and a Kevlar-29 / epoxy backing plate of an 8 mm thickness as shown in Figure 2b. The areal density of the composite structure is 39 kg/m^2. This armor is manufactured by first cutting Kevlar-29 / epoxy prepreg laminates according to the required size; then adding a polyurethane adhesive layer with a thickness of 1 mm before stacking the ceramic tile on the adhesive layer. During the fabrication process, the specimen is checked thoroughly to assure no gaps or voids in the assembled parts.

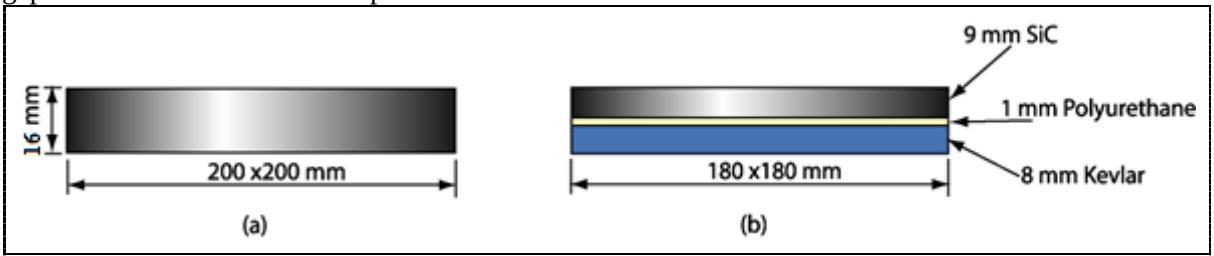

Figure 2. (a) ARMOX 500T Plate and (b) Bilayer Composite Plate

2.1.3. Experimental procedure. For the present work, the above fabricated specimens are subjected to 7.62 x 54 mm API projectiles at 810 m/s impact velocity in the lab. According to Fayed et al. [11], the

test lab was adjusted according to NIJ 0101.06 Level IV standard and the projectiles were fired in a test barrel. Two sensor sets were adjusted to measure the velocity of the projectiles. The target is clamped at the peripherals, with an exposed area of 175 × 175 mm. A schematic diagram of the firing range is shown in Figure 3.

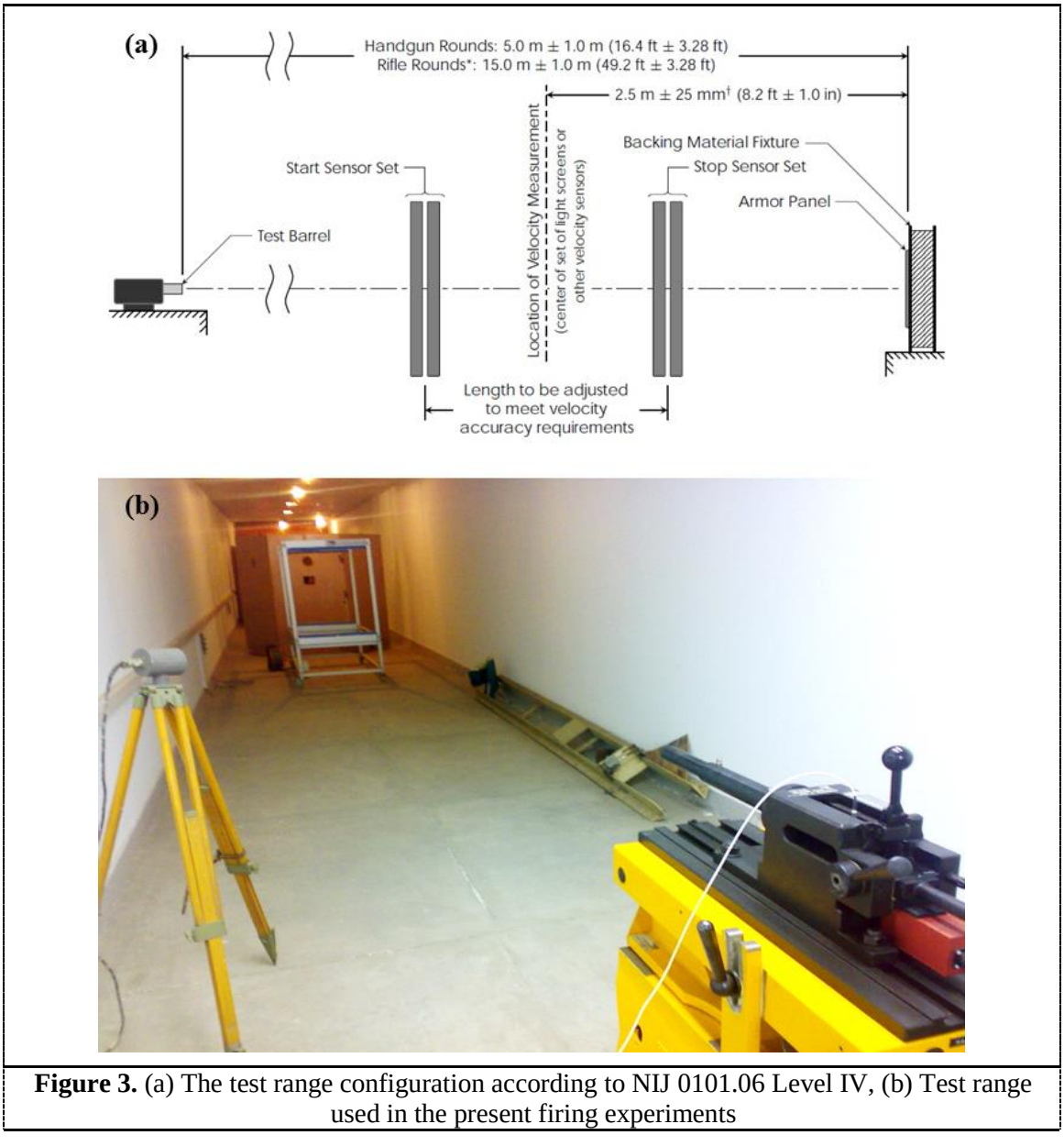

Figure 3. (a) The test range configuration according to NIJ 0101.06 Level IV, (b) Test range used in the present firing experiments

2.2. FEA Modelling

2.2.1. Modelling details. 3D FE models have been developed using FEA software package. The objective is to investigate the effect of composite bilayer armor structure on bullet penetration as compared to ARMOX 500T armor and the gained mass reduction. In the present work, a Polyurethane layer was used as an adhesive layer between ceramic tile and backing plate, and considered to be completely bonded to both surfaces. The bond strength of the adhesive layer might vary as a result of several manufacturing settings. Therefore, the present FEA simulations are conducted at a normal strength of 93 MPa and a shear strength of 45.8 MPa [1].

Figure 4 shows the FEA models of the two cases. Because of the two orthogonal planes of symmetry of the composite laminates, only one-quarter of the armors and the projectiles are modelled to save computational costs. These models resulted in a total of 20,973 nodes for the symmetric model of bare ARMOX 500T armors by using C3D8R (An 8-node linear brick, reduced integration, hourglass control) elements, and a total of 51,231 nodes by using C3D8R elements for the symmetric model of the composite bilayer armor structure.
To define the boundary conditions for one-quarter FEA model, We use three boundary conditions, the first one is for the armor to fix it from its outer edges completely (i.e. U1=U2=U3=UR1= UR2=UR3=0), the second is to define the first symmetrical plane (YZ Plane) for the armor and projectile (i.e. U1= UR2=UR3=0), and the last one is to define the second symmetrical plane (XZ Plane) for the armor and projectile (i.e. U2= UR1=UR3=0) .
Verification experiments were conducted to compare between FEA and experimental results.

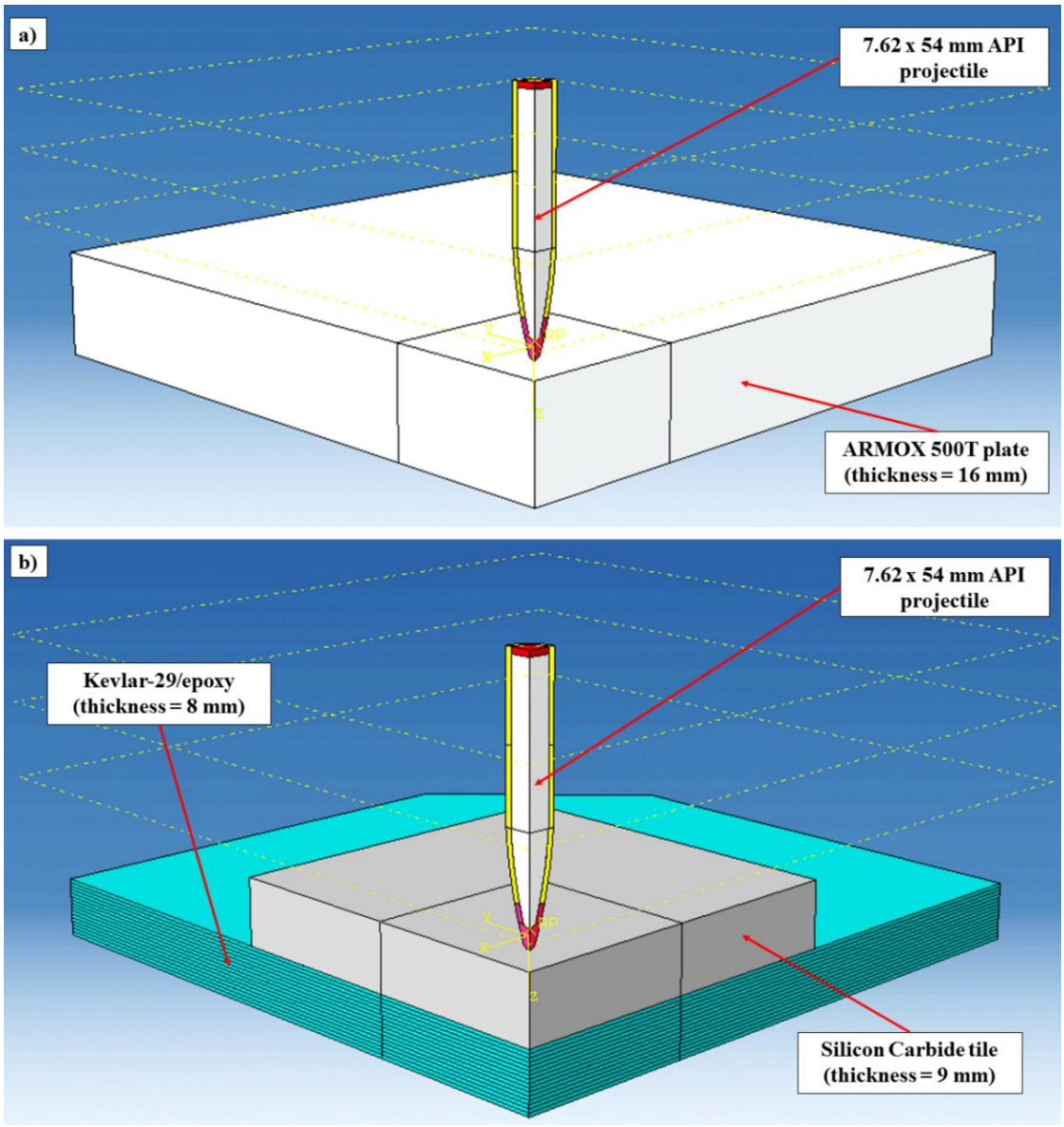

Figure 4. Quarter symmetrical models of the armors used in FEA simulations, (a) Bare of 16 mm thickness ARMOX 500T armor, (b) Composite bilayer armor structure

2.2.2. Material Constitutive Models.

2.2.2.1 Projectile material model. In the present work, the Johnson-Cook (JC) constitutive model [12], was utilized to describe the behavior of the nose filler, jacket, and core of the projectile. The stress-strain relationship is given as:

$$\sigma_y\left(\varepsilon_p.\dot{\varepsilon_p}.T\right) = \left(A + B\,\varepsilon_p^n\right)\left(1 + C\,ln\,\dot{\varepsilon_p^*}\right)(1 - T^{*m}) \quad (1)$$

where σ_y is the yield stress, ε_p, $\dot{\varepsilon_p}$ are equivalent plastic strain and equivalent plastic strain rate respectively. $\dot{\varepsilon_p^*}$ Can be calculated as

$$\dot{\varepsilon_p^*} = \frac{\dot{\varepsilon_p}}{\dot{\varepsilon_0}} \quad (2)$$

where $\dot{\varepsilon_0}$ designates the reference strain rate. Also, the homologous temperature T^* can be defined as

$$T^* = \frac{(T - T_0)}{(T_m - T_0)} \quad (3)$$

where T^*, T, T_0, and T_m are the homologous temperature, working temperature, reference temperature, and melting temperature respectively.

Moreover, n is the exponent of strain hardening, m is the exponent of temperature softening, A is the yield stress constant, B is the strain hardening constant, and C is a material constant.

The J-C parameters of the projectile components are obtained from relevant literature. Specifically, the jacket and core material parameters are obtained from Anderson et al. [10], and lead filler parameters are taken from Fras et al. [13]. The J-C parameters are summarized in Table 1.

A criterion for element erosion that governs the projectile's erosion is used in the present FEA simulation, the equivalent plastic strain is used to estimate the erosion. According to Anderson et al. [10] and Fras et al. [13], the equivalent plastic strain values for the jacket, lead filler, and core are 200%, 100%, and 10%, respectively.

Table 1. Parameters of the projectile materials according to Johnson-Cook (J-C) model

Parameter	Notation	Lead [13]	Jacket [10]	Core [10]
Young's modulus	E [GPa]	17.156	124.9	210
Poisson's ratio	ν	0.44	0.35	0.29
Density	$\boldsymbol{\rho}$ [Kg/m^3]	11340	8940	7800
Yield stress constant	A [GPa]	0.024	0.5	1.034
Strain hardening constant	B [GPa]	0.3	0	18.095
Strain rate constant	C	0	0.025	0.005
Thermal softening constant	m	1.0	1.0	1.0
Strain hardening exponent	n	0.59	1.0	0.64
Melting temperature	T_m [K]	760	1360	1790
Reference strain rate	$\dot{\varepsilon}_0$[s^{-1}]	1.0	1.0	1.0
Failure equivalent plastic strain	FS	100 %	200 %	10 %

Based on the fracture criterion of Johnson et al. [12], Hancock et al. [14] extended this criterion by including the failure strain sensitivity to temperature, strain rate, strain path, and stress triaxiality. The model assumed that damage builds up in the material elements during plastic straining, and accelerates when it reaches a critical value. If D defines the damage state, elements that are entirely damaged are referred to as D = 1, otherwise the undamaged elements will be identified as D = 0. Failure is defined as the condition that D equals or surpasses the value of unity.

$$D = \sum \frac{\Delta \varepsilon_{pl}}{\varepsilon_{p.f}} \tag{4}$$

where $\varepsilon_{p.f}$ is the equivalent plastic strain at failure, and $\Delta \varepsilon_{pl}$ is an increment of the equivalent plastic strain; the sum of these values is estimated across all deformation increments. Nevertheless, the damage variable's critical value, (i.e. the value at which the micro-cracks initiated is less than one). Thus, the following is the failure criterion:

$$D = D_c \leq 1 \tag{5}$$

In addition, earlier studies show that the damage value stays equal to zero as dislocations accumulate and initiate micro-cracks. There might be a certain value for the total plastic strain at which damage begins to develop. These earlier investigations allow for the proposal of the following damage rule:

$$\dot{D} = \begin{cases} 0 & , when\ \varepsilon_{pl} < \varepsilon_{p.d} \\ \frac{D_c}{\varepsilon_f - \varepsilon_{fp.d}}\ \dot{\varepsilon}_{pl} & , when\ \varepsilon_{pl} \geq \varepsilon_{p.d} \end{cases} \tag{6}$$

where D_c is the critical damage, $\varepsilon_{p.d}$ is the damage threshold and ε_f is the fracture strain, and the fracture is started by void nucleation. A linear function of equivalent plastic strain termed the damage growth law is given by:

$$\dot{D} = \frac{D_{c1}}{\varepsilon_{p0}}\ \dot{\varepsilon}_{p.eq} \tag{7}$$

Here, ε_{p0} is the plastic strain and D_{c1} is the initiation of necking and is assumed to equal 2%. Void growth causes the damage to grow more quickly during the necking phase after the ultimate point. At this point, the damage is growing nonlinearly and can be expressed as:

$$\dot{D} = \frac{\frac{D_{c2} - D_{c1}}{D_{c2} - D}}{\varepsilon_{p.f} - \varepsilon_{p0}}\ \dot{\varepsilon}_{p.eq} \tag{8}$$

Here, D_{c2} is critical damage at fracture and taken as 0.8, $\varepsilon_{p.f}$ is the strain at failure and expressed as:

$$\varepsilon_f = [D_1 + D_2 \exp(D_3 \sigma^*)] \left[1 + D_4 ln\left(\dot{\varepsilon_p}^*\right)\right] [1 + D_5 T^*] \tag{9}$$

The model by Johnson et al. [12] stated that ε_f depends on stress triaxiality, temperature, and strain rate, where D_1 to D_5 are material constants, σ_m is the mean stress, $\sigma^* = \frac{\sigma_m}{\sigma_{eq}}$ is the stress triaxiality ratio and or hydrostatic stress. Given that the material strength decreases during deformation due to damage, the constitutive equation for the damaged material can be expressed as:

$$\sigma_D = (1 - D)\, \sigma_{eq} \tag{10}$$

where, σ_D is the stress at the damaged state and σ_{eq} for the original (undistorted) material was previously estimated in equation (4).

The failure model defined in equations (4) through (10) is implemented in the FEA software. The stress components are set to zero when meet the failure criterion, and they stay at zero for the duration of the FEA simulation. The mesh's failing elements are deleted by the FE code. The used ARMOX 500T (J-C) model parameters are summarized in Table 2.

Table 2. JC model parameters of the ARMOX 500T material [15]

Parameter	Notation	Value
Young's modulus	E [GPa]	210
Poisson's ratio	ν	0.33
Density	$\boldsymbol{\rho}$ [Kg/m^3]	7850
Yield stress constant	A [GPa]	0.286
Strain hardening constant	B [GPa]	1.510
Strain rate constant	C	0.0087
Thermal softening constant	m	1.04496
Strain hardening exponent	n	0.02482
Melting temperature	T_m [K]	1800
Specific heat	C_p [J/kg·K]	452
Reference strain rate	$\dot{\varepsilon}_0$[s^{-1}]	1.0
Inelastic heat fraction	χ	0.9
Expansion coefficient	α	1.2 x 10^{-5}
Fracture strain model constants	D1	0.068
	D2	5.328
	D3	-2.554
	D4	0
	D5	0

2.2.2.2 Ceramic material model. In the present FEA simulation, the Johnson-Holmquist (JH2) model was chosen to investigate the material behavior of ballistic ceramics. The Johnson-Holmquist (JH2) strength model described by Islam et al. [16] can be stated as follows:

$$\sigma^* = \sigma_i^* - D(\sigma_i^* - \sigma_f^*) \tag{11}$$

$$\sigma_i^* = A(P^* + T^*)^N \left(1 + C\ ln\ \dot{\varepsilon_p^*}\right) \tag{12}$$

$$\sigma_f^* = B(P^*)^M \left(1 + C\ ln\ \dot{\varepsilon_p^*}\right) \tag{13}$$

$$\varepsilon_f^p = D_1(P^* + T^*)^{D_2} \tag{14}$$

$$P = K_1\,\mu + K_2\,\mu^2 + K_3\,\mu^3 + \Delta P\mu \geq 0 \tag{15}$$

To manage the element erosion, an equivalent plastic strain value was assumed to be 0.25 to provoke acceptable material distortion. The elements that meet the criteria will be eliminated. The parameters of Johnson-Holmquist (JH2) model are summarized in Table 3.

Table 3. JH2 model parameters of Silicon Carbide [16]

Parameter		Notation	Value
Tensile strength		T[GPa]	0.37
Pressure constants	Bulk modulus	K1 [GPa]	204.785
	Second pressure coefficient	K2 [GPa]	0
	Third pressure coefficient	K3 [GPa]	0
Bulking factor		β_f	1.0
Hugoniot elastic limit		HEL[GPa]	14.567

Table 3. JH2 model parameters of Silicon Carbide [16]

Parameter	Notation	Value
Pressure at Hugoniot elastic limit	P_{HEL} [GPa]	5.9
Strength at Hugoniot elastic limit	σ_{HEL} [GPa]	13
Maximum normalized fractured strength	σ_{max}^{f} [GPa]	0.8
Intact strength constant	A	0.96
Fractured strength constant	B	0.35
Strain rate constant	C	0
Fractured strength exponent	M	1
Intact strength exponent	N	0.65
Damage coefficients	D1	0.48
	D2	0.48

2.2.2.3 Kevlar-29 / epoxy composite material model. The armor's backing plate is made of a Kevlar-29 reinforced epoxy composite. A single-layer Kevlar-29 fabric has a plain weave structure with two in-plane orthogonal directions that have identical mechanical properties, with a thickness of 0.5 mm. To produce the required thickness, many layers of the composite were piled on top of each other. The mechanical properties in the thickness direction are lower than in the other two directions as a result of the low strength of the epoxy. An orthotropic elastic model is employed in the finite element model. Nevertheless, fiber-reinforced polymer composites may be subject to damage after impacts, including interlayer delamination, matrix cracking, and fiber breaking.

In the present work, a user subroutine VUMAT was used to implement a Hashin damage initiation criterion [17] in FEA software, which takes into account the Kevlar-29 structure's bi-directional strength. However, Tan et al. [18] estimated the damage of the Kevlar-29 fabric composites according to the following equations:

Tensile damage in the 1st fiber direction if $d_{ft1} > 1$, where

$$d_{ft1} = \left(\frac{\sigma_1}{X_{1t}}\right)^2, \sigma_1 > 1 \tag{16}$$

Compressive damage in the 1st fiber direction if $d_{fc1} > 1$, where

$$d_{fc1} = \left(\frac{\sigma_1}{X_{1c}}\right)^2 + \left(\frac{\tau_{12}}{S_{12}}\right)^2 + \left(\frac{\tau_{13}}{S_{13}}\right)^2, \sigma_1 > 1 \tag{17}$$

Tensile damage in the 2nd fiber direction if d_{ft2}, where

$$d_{ft2} = \left(\frac{\sigma_2}{X_{2t}}\right)^2, \sigma_2 > 1 \tag{18}$$

Compressive damage in the 2nd fiber direction if d_{fc2}, where

$$d_{fc2} = \left(\frac{\sigma_2}{X_{2c}}\right)^2 + \left(\frac{\tau_{12}}{S_{12}}\right)^2 + \left(\frac{\tau_{23}}{S_{23}}\right)^2, \sigma_1 > 1 \tag{19}$$

Tensile damage in the thickness direction if $d_{mt} > 1$, where

$$d_{mt} = \left(\frac{\sigma_3}{X_{3t}}\right)^2 + \left(\frac{\tau_{13}}{S_{13}}\right)^2 + \left(\frac{\tau_{23}}{S_{23}}\right)^2, \sigma_3 > 0 \tag{20}$$

Compressive damage in the thickness direction if $d_{mc} > 1$, where

$$d_{mc} = \left(\frac{\sigma_3}{X_{3c}}\right)^2 + \left(\frac{\tau_{13}}{S_{13}}\right)^2 + \left(\frac{\tau_{23}}{S_{23}}\right)^2, \sigma_3 < 0 \tag{21}$$

The 1st and 2nd directions in the previous formulations correspond to the two perpendicular in-plane directions, and the 3rd direction corresponds to the out-of-plane direction. The corresponding strength is the denominator of the terms, and the numerators are the stress levels computed in each respective direction. Based on the calculations of the fracture energy dissipation during the damage process, damage evolution in the corresponding direction is identified once the damage initiation

requirement has been satisfied. A damage evolution law was defined that was comparable to the one put by Lapczyk et al. [19]. A fracture energy of 12.5 N/mm is chosen. The Mechanical properties of Kevlar-29 / epoxy are summarized in Table 4.

Delamination and debonding model. The Kevlar-29 backing plate is made from multiple plies of Kevlar-29 fabrics assembled using an epoxy matrix. On the other hand, the ceramic tile was mounted onto the backing plate using a Polyurethane layer. This indicates that delamination could happen at the interface where the backing plate and ceramic tile meet, as well as in between the Kevlar-29 plies. In FEA software code, this failure is modelled using surface-based cohesive behavior. In particular, the bonding layer interface fails when the maximum cohesive stress damage initiation value equals one as follows:

$$max\left\{\frac{\langle t_n \rangle}{t_n^0}.\frac{t_s}{t_s^0}.\frac{t_t}{t_t^0}\right\} = 1 \quad (22)$$

where t_n, t_s, and t_t are cohesive stresses at the normal and the shear directions, respectively, and t_n^0, t_s^0, and t_t^0 represent the normal and shear strengths in directions 1 and 2, respectively. In the current FE simulation, the normal strength is 93 MPa while the shear strength is 45.8 MPa.

Table 4. Mechanical properties of Kevlar-29 / epoxy [1]

Parameter	Notation	Value
Density	$\boldsymbol{\rho}$ [Kg/m^3]	1259
Young's modulus in direction 1	E_1 [GPa]	20.5
Young's modulus in direction 2	E_2 [GPa]	20.5
Young's modulus in direction 3	E_3 [GPa]	6
Poisson's ratio in direction 12	ν_{12}	0.21
Poisson's ratio in direction 13	ν_{13}	0.33
Poisson's ratio in direction 23	ν_{23}	0.33
Tensile strength in direction 1	X_{1t} [GPa]	0.685
Tensile strength in direction 2	X_{2t} [GPa]	0.685
Tensile strength in direction 3	X_{3t} [GPa]	12
Compressive strength in direction 1	X_{1c} [GPa]	0.685
Compressive strength in direction 2	X_{2c} [GPa]	0.685
Compressive strength in direction 3	X_{3c} [GPa]	12
Shear modulus in direction 12	G_{12} [GPa]	0.77
Shear modulus in direction 13	G_{13} [GPa]	2.71
Shear modulus in direction 23	G_{23} [GPa]	2.71
Shear strength in direction 12	S_{12} [GPa]	0.077
Shear strength in direction 13	S_{13} [GPa]	0.542
Shear strength in direction 23	S_{23} [GPa]	0.542

3. Results and Discussions

Impact simulations were conducted for two different armor structures with and without a ceramic front layer, at an impact velocity equal to 810 m/s. It was observed that the penetration resistance of the lighter composite armor was better than the heavier ARMOX 500T plate. While the projectile was completely arrested by the first ARMOX 500T armor, the other one succeeded in bouncing the projectile backward after impact with minimum back trauma. In a parallel procedure, all the laboratory experiments were simulated on the FEA software package with accepted converged results.

The developed FE models captured the global ballistic performance of the armors in terms of penetration resistance. It is regarded as an appropriate technique for examining the current topic. Figures 5 to 9 show projectiles' penetration in both samples. Specifically, for the 16 mm thickness bare ARMOX 500T plate, the specimen was partially penetrated as shown in Figure 5. Also, for the composite bilayer armor structure, the specimen was not penetrated. In other words, the lighter composite bilayer armor structure can resist 7.62 x 54 mm API projectiles better than the heavier and thicker ARMOX 500T armor as shown in Figures 7 and 8.

The present FE models could investigate the dissipated energy by each component, and plots of the evolution of internal and kinetic energy have been generated for each case as shown in Figures 6 and 9.

Figures 6a and 6b show, for the case of bare ARMOX 500T armor with a thickness of 16 mm, a major part of the projectile's kinetic energy is transformed into internal energy in the armor and the projectile itself. However, a small amount of the projectile's kinetic energy was still maintained in the projectile's debris. Nevertheless, the armor arrested the rest of the eroded projectile core after impact as shown in Figure 5d.

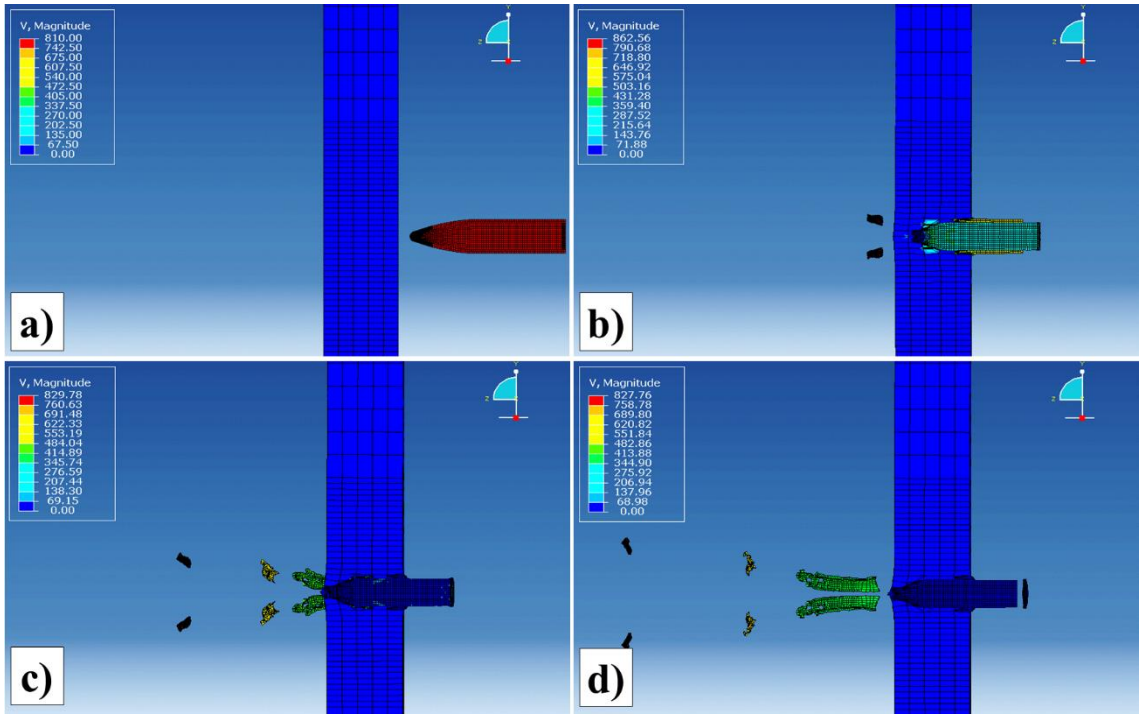

Figure 5. Ballistic performance of the 16 mm thickness ARMOX 500T armor against 7.62 x 54 mm API Projectiles at different times, (a) 0 μs; (b) 33 μs ; (c) 66 μs; and (d) 100 μs

We noticed that the projectile's velocity is fluctuating as shown in Figures 6c, we assume this happens because of the way we define the projectile's velocity during the impact. A single point (i.e. the core tip) is determined to measure the projectile's velocity during impact. When some parts of the projectile break during impact, the mass of the part where the measurement point is located changes in a small percentage, affecting its kinetic energy and therefore its velocity. But, in general, the velocity of the projectile tends to decrease due to the resistance of the armor.

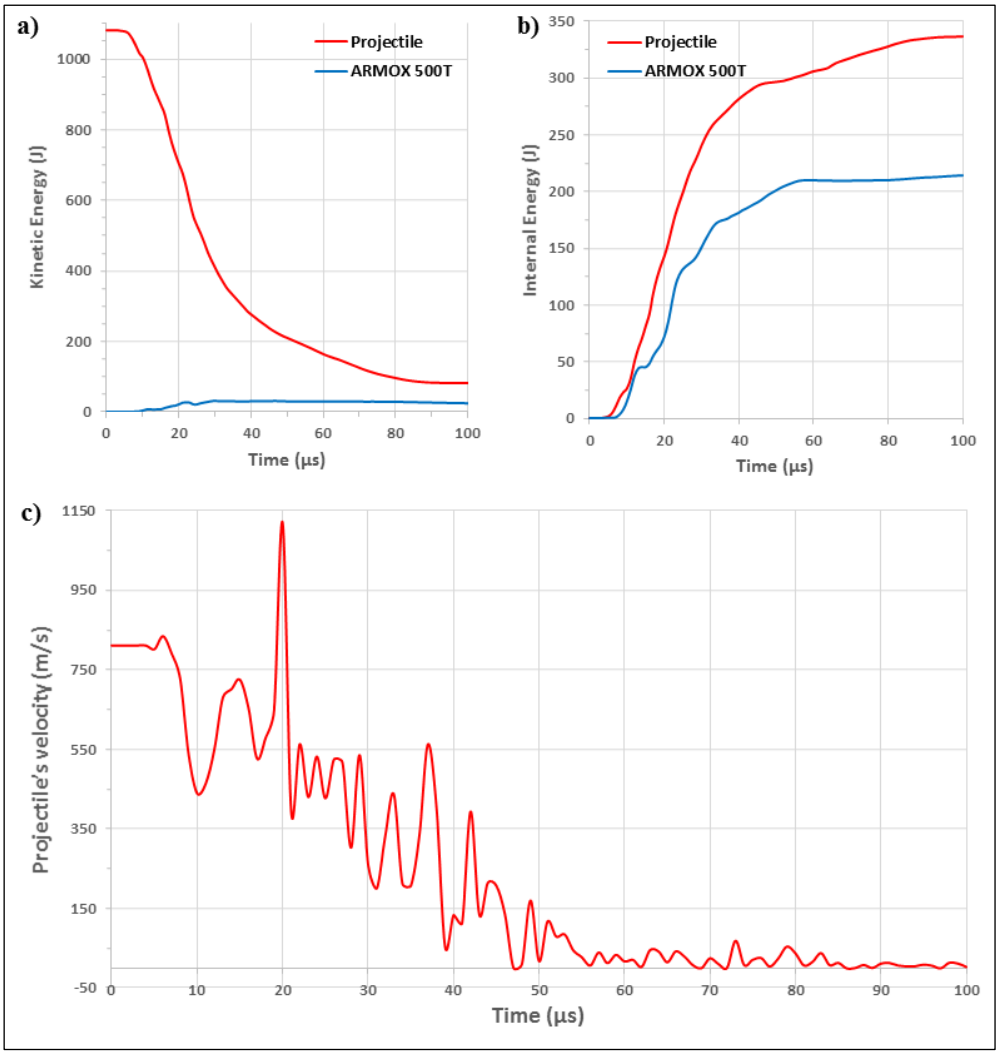

Figure 6. Time history of impact simulation against ARMOX 500T armor with thickness = 16 mm, (a) kinetic energy, (b) internal energy, (c) Projectile's core velocity

For the other kind of tested armor, the Composite specimen after impact in the firing range is shown in Figures 7 and 8. An adhesive surface contact was designed to simulate the interaction between different layers of the composite armor. The present FE models captured the failure of the adhesive layer interface. It was investigated that the interface always initiates at the hit point and propagates to the peripherals. On the other hand, the projectile's core velocity could be measured by FEA software to study and analyze the performance of the two armors. The impact velocity of the projectile in this study is 810 m/s. Similarly, the dissipated energy by each component could be investigated, and plots of the historical evolution of internal and kinetic energy have been generated for each case as shown in Figure 9.

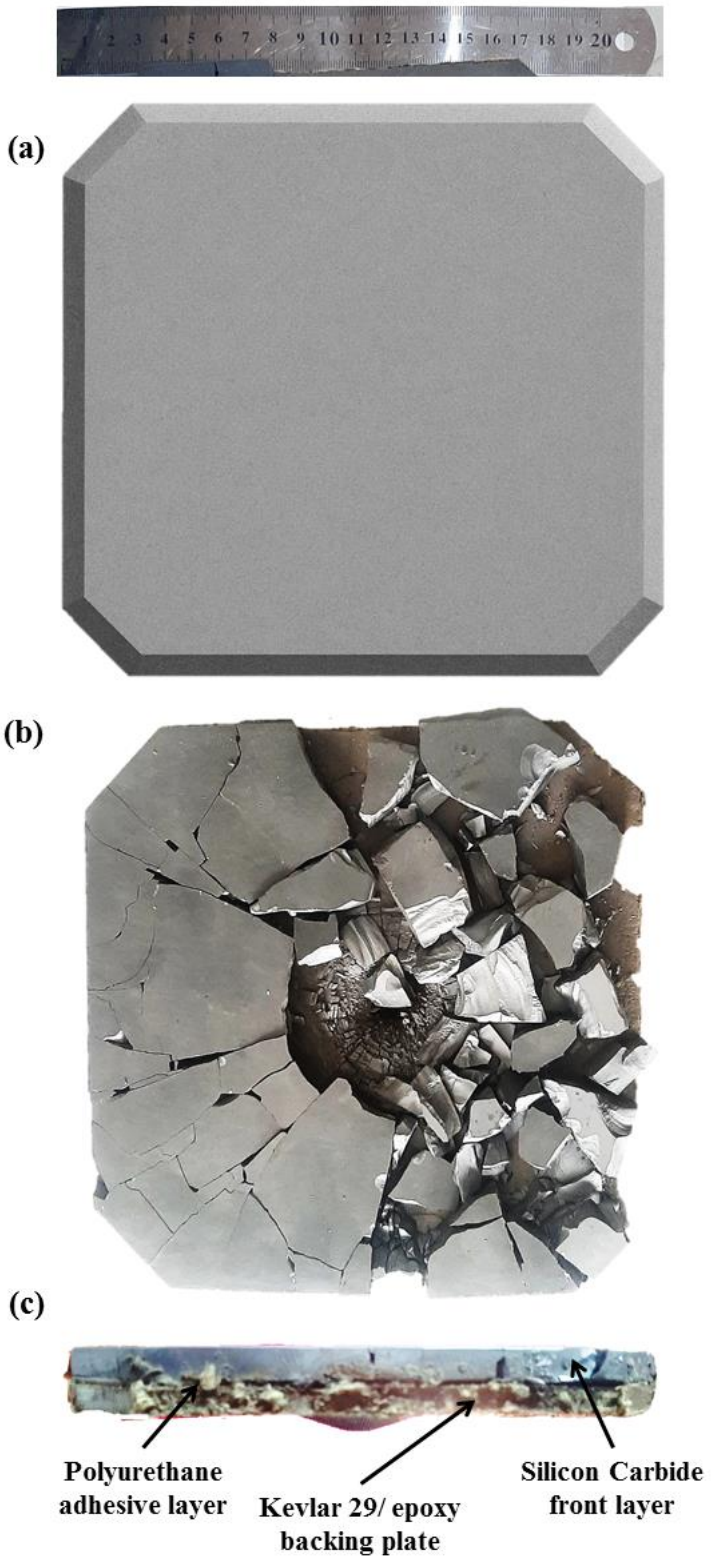

Figure 7. (a) Front view of the bilayer armor structure before impact, (b) Front view of the bilayer armor structure after impact (c) Section view of the composite bilayer armor structure after impact

Similarly, the Composite specimen was simulated during firing of 7.62 x 54 mm API projectile as shown in Figures 7.

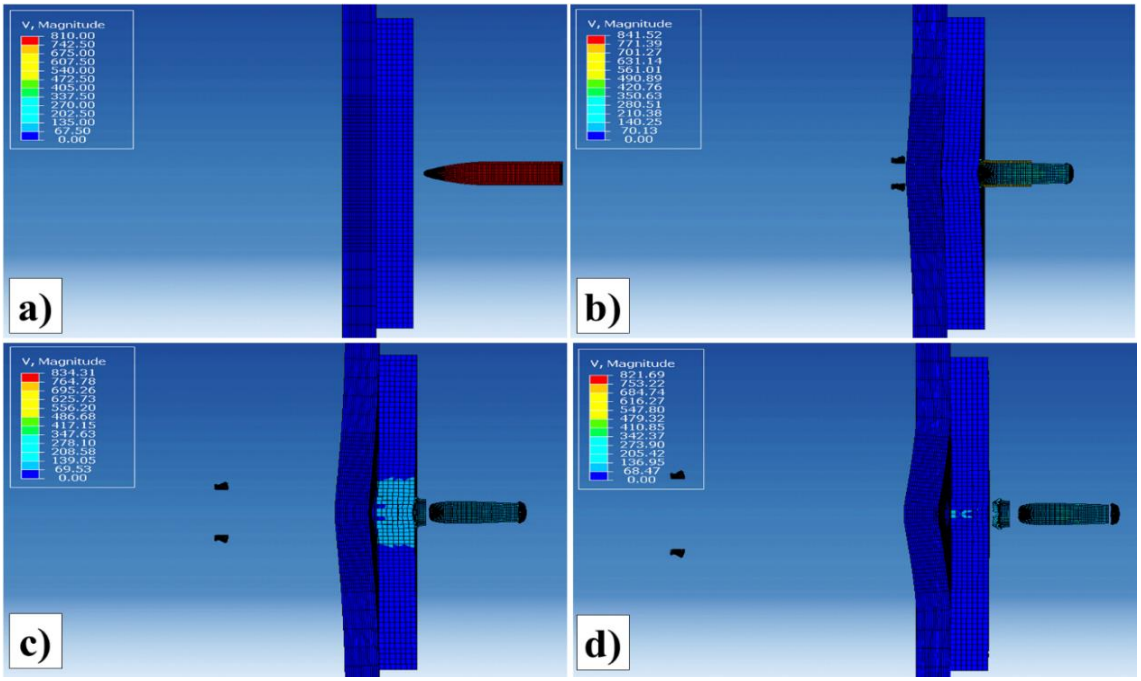

Figure 8. Ballistic performance of the composite bilayer armor structure against 7.62 x 54 mm API Projectiles at different times, (a) 0 μs; (b) 33 μs; (c) 66 μs; and (d) 100 μs

Figures 9a and 9b show, in the case of the composite bilayer armor structure, a major part of the projectile's kinetic energy is transformed into kinetic energy but in the opposite direction after bouncing. The armor bounced the rest of the eroded projectile core and debris after impact as shown in Figure 8d.

The ceramic tiles contribute to the absorption of the projectile's kinetic energy, which indicates that the ceramic tiles play an important role in the dissipation of the projectile's kinetic energy. Also, the Polyurethane adhesive layer and bonding between successive Kevlar-29 layers dissipated a small portion of the projectile's kinetic energy, even when the amount is limited when compared to other armor elements. This observation indicated that the adhesive layers affected the backing plate's ability to dissipate energy. Therefore, in the present work, the backing plate absorbs less energy than in the bare case, i.e., the ballistic performance is improved for this kind of armor structure.

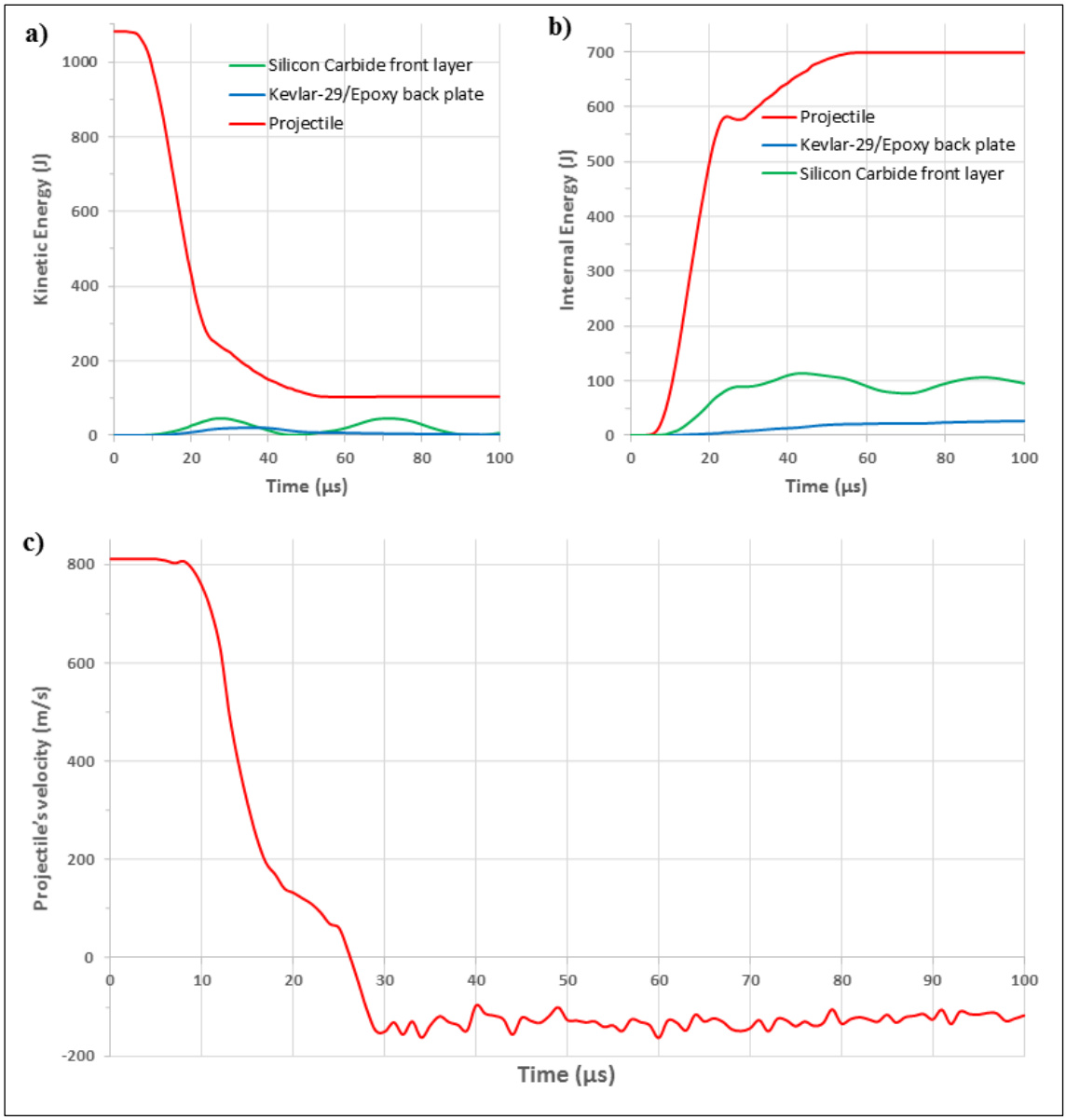

Figure 9. Time history of impact simulation against bilayer composite armor structure, (a) kinetic energy, (b) internal energy, (c) Projectile's core velocity

The present FE models captured the failure of the adhesive layer interface. It is evident that the interface failure always initiates at the hit point and propagates to the peripherals. Figure 10 shows a contour plot for damage spread upon impact at the cohesive surfaces representing the bonding between different layers. The colored contours represented the value of damage initiation as stated in Eq. (22), traced at the adhesive layer's upper surface, where it adhered to the Silicon Carbide tile, with the blue color indicating complete bonding through the red color indicating failure of the adhesive layer.

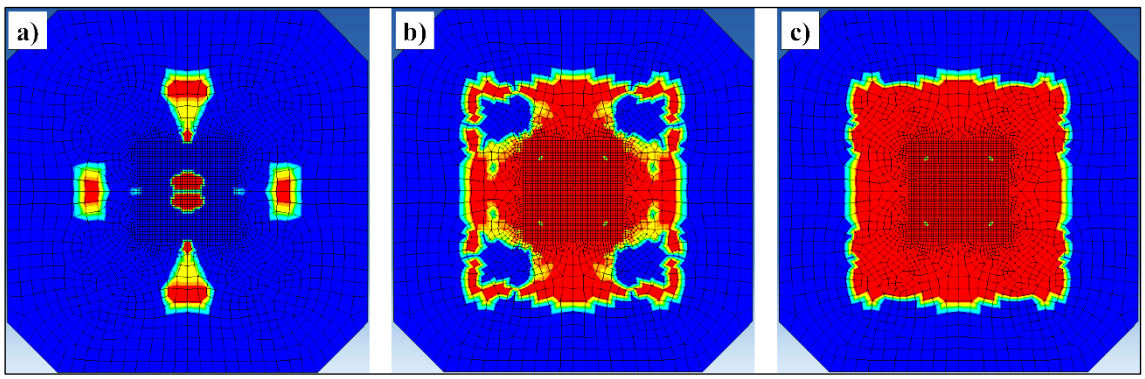

Figure 10. Interface failure extent on the adhesive layer at different time instants (a) 10 µs; (b) 20 µs; (c) 40 µs

4. Conclusions

- Compared to the ARMOX 500T armors, experimental and FEA simulation results suggest that by adding a front Silicon Carbide layer to a Kevlar-29 / epoxy backing plate, the aerial density decreases by 69 % and the kinetic energy dissipated from the projectile was increased by about 2.22 % with better ballistic performance against 7.62 x 54 mm API Projectiles.
- The improved ballistic performance is associated with the following: (1) the energy dissipation by the front layer and the adhesive layer; and (2) the erosion of the projectile caused by the front ceramic layer.
- The FEA simulation revealed that the bond strength between the different layers of the armor system could affect the penetration behavior, In order to confine the debris and disperse the projectile's kinetic energy, a higher bond strength is preferable. This may be an opportunity to improve the ballistic performance of composite lightweight armors by further investigations.
- The developed FE model has been validated against the experimental work and could be used for optimization of composite bilayer armor in future studies.

References

[1] Guo G, Alam S and Peel L D 2022 An investigation of deformation and failure mechanisms of fiber-reinforced composites in layered composite armor. Composite Structures, **281, 115125.** https://doi.org/10.1016/j.compstruct.2021.115125

[2] Shaker M, Abou-Elela H Riad, A, and Fayed A 2012 Numerical investigation of a high-speed projectile penetration into bi-layered lightweight targets. The International Conference on Applied Mechanics and Mechanical Engineering, **15(15), 1–17.** https://doi.org/10.21608/amme.2012.37259

[3] Senthil, K, Iqbal, M, & Gupta, N 2017 Ballistic resistance of mild steel plates of various thicknesses against 7.62 AP projectiles. International Journal of Protective Structures, **8(2), 177–198.** https://doi.org/10.1177/2041419617700007

[4] Abou-Elela, H, Riad, A, Fayed, A, & Shaker, M 2012 Modeling penetration of bi-element metallic targets by high-speed projectiles. The International Conference on Applied Mechanics and Mechanical Engineering, **15(15), 1–18.** https://doi.org/10.21608/amme.2012.37260

[5] Fayed, A I H, Abo El Amaim, Y A, Ramy, O, & Elgohary, D H 2021 Assessment of the mechanical properties of different textile materials used for outer shell of bulletproof vest: Woven fabrics for military applications. Research Journal of Textile and Apparel, **27(1), 1–18.** https://doi.org/10.1108/rjta-03-2021-0027

[6] Gregori, D, Scazzosi, R, Nunes, S G, Amico, S C, Giglio, M, & Manes, A 2020 Analytical and numerical modelling of high-velocity impact on multilayer alumina/aramid fiber composite ballistic shields: Improvement in modelling approaches. Composites Part B: Engineering, **187, 107830.** https://doi.org/10.1016/j.compositesb.2020.107830

[7] Meng, S, Taddei, L, Lebaal, N, & Roth, S 2021 Advances in ballistic penetrating impact simulations on thin structures using smooth particles hydrodynamics: A state of the art. Thin-Walled Structures, **159, 107206.** https://doi.org/10.1016/j.tws.2020.107206

[8] Fayed, A 2024 Developments of 7.62 X39MM armor piercing projectiles. Journal of Physics: Conference Series, **2811(1), 012026.** https://doi.org/10.1088/1742-6596/2811/1/012026

[9] Chocron, S, Anderson, C E, Grosch, D J, & Popelar, C H 2001a Impact of the 7.62-mm API projectile against the edge of a metallic target. International Journal of Impact Engineering, **25(5), 423–437.** https://doi.org/10.1016/s0734-743x(00)00063-4

[10] Anderson, Jr, Charles & Burkins, Matthew & Walker, James & Gooch, William 2005 Time-Resolved Penetration of B_4C Tiles by the APM2 Bullet. CMES - Computer Modeling in Engineering and Sciences. **8. 91-104.**

[11] Fayed, A, Elawad, E, & Abdelkader, M 2011 Ballistic resistance of flexible composite (Kevlar-129/line-X XS 350). International Conference on Aerospace Sciences and Aviation Technology, 11(ASAT CONFERENCE), **1–15.** https://doi.org/10.21608/asat.2011.27153

[12] Johnson, G R, & Cook, W H 1985a Fracture characteristics of three metals subjected to various strains, strain rates, temperatures and pressures. Engineering Fracture Mechanics, **21(1), 31–48.** https://doi.org/10.1016/0013-7944(85)90052-9

[13] Fras, T, Murzyn, A, & Pawlowski, P 2017 Defeat mechanisms provided by slotted add-on bainitic plates against small-calibre 7.62 mm × 51 AP projectiles. International Journal of Impact Engineering, **103, 241–253.** https://doi.org/10.1016/j.ijimpeng.2017.01.015

[14] Hancock, J W, & Mackenzie, A C 1976 On the mechanisms of ductile failure in high-strength steels subjected to multi-axial stress-states. Journal of the Mechanics and PhySilicon Carbides of Solids, **24(2–3), 147–160.** https://doi.org/10.1016/0022-5096(76)90024-7

[15] Saleh, M, Luzin, V, Kariem, M A, Thorogood, K, & Ruan, D 2019 Experimental measurements of residual stress in Armox 500t and evaluation of the resultant ballistic performance. Journal of Dynamic Behaviour of Materials, **6(1), 78–95.** https://doi.org/10.1007/s40810-019-00231-w

[16] Islam, M R, Zheng, J Q, & Batra, R C 2020 Ballistic performance of ceramic and ceramic-metal composite plates with JH1, JH2 and JHB material models. International Journal of Impact Engineering, **137, 103469.** https://doi.org/10.1016/j.ijimpeng.2019.103469

[17] Hashin, Z 1981 Fatigue failure criteria for unidirectional fiber composites. Journal of Applied Mechanics, **48(4), 846–852.** https://doi.org/10.1115/1.3157744

[18] Tan, L B, Tse, K M, Lee, H P, Tan, V B, & Lim, S P 2012 Performance of an advanced combat helmet with different interior cushioning systems in ballistic impact: Experiments and finite element simulations. International Journal of Impact Engineering, **50, 99–112.** https://doi.org/10.1016/j.ijimpeng.2012.06.003

[19] Lapczyk, I, & Hurtado, J A 2007 Progressive damage modeling in fiber-reinforced materials. Composites Part A: Applied Science and Manufacturing, **38(11), 2333–2341.** https://doi.org/10.1016/j.compositesa.2007.01.017